Eur. Phys. J. E (2014) **37**: 88
DOI 10.1140/epje/i2014-14088-y

THE EUROPEAN PHYSICAL JOURNAL E

Regular Article

Dual fragmentation modes of the explosively dispersed granular materials

Kun Xue[a], Qiqi Yu, and Chunhua Bai

The Key State Laboratory of Explosion Science and Technology, Beijing Institute of Technology, Beijing, 100081, China

Received 4 April 2014 and Received in final form 27 June 2014

Published online: 30 September 2014 –

Abstract. Granular materials subjected to blast loading caused by a central explosion exhibit a distinctive dual jetting phenomenon. A large number of fine particle jets are ejected from the outer edge of the charge upon the reflection of the shock wave from the free surface, and are soon overtaken and overlapped by a second set of much thicker particle jets from the inner edge. Our numerical studies suggest that these two distinct sets of particle jets arise from a subsequent fragmentation of the outer and inner particle layers formed during shock interaction. The instability onset of the inner particle layer, which remains intact after the spallation of the outer particle layer, corresponds to the destabilizing viscous forces prevailing over the stabilizing inertial forces. The physical mechanism responsible for the spallation of the outer particle layer is accounted for by a three-phase cavitation model consisting of nucleation, unconditioned and conditioned growth of voids. The theoretically predicted fragmentation onset and fragment size are well consistent with the experimental results. Moreover, by incorporating the moisture effect into the granular material model, results of the cavitation model indicate an increased number of jets generated by saturated particles, as observed in experiments. With minor shock energy being consumed on the saturated particle compaction thanks to the remarkably low compressibility of saturated particles, the shock wave retains the steep front during propagation and subsequently produces a sharp reflection wave leading to a considerably higher strain relaxation rate in saturated particles than that in dry particles. The pressure relaxation duration prescribes the time the activated nucleation sites are allowed to communicate with each other. Consequently nucleation sites in saturated particles have more chances to survive and fully develop than those in dry particles giving rise to smaller fragments.

1 Introduction

Dynamic fragmentation of explosive loaded multi-phase granular materials is of significance to both basic science and a variety of military and engineering applications, such as landmines, thermobaric (metalized) explosives (TBX) and blast mitigants [1–7]. Extensive research work, both theoretical and experimental, has been dedicated to the explosive dispersal of granular matters, including the widely observed formation of post-detonation "particle" jets whose leading edges are agglomerates of constituent grains [4–9]. The size and number of these jets are important to the viability of many applications, specifically, through controlling the jets mixing and thus the late-time combustion process of the TBX [9] or determining the efficiency of energy transfer from the blast wave to the disseminated particles in the case of blast mitigation [4].

As opposed to the premixed explosive and particles, particles surrounding the central explosive interestingly exhibit a dual jetting structure, which becomes more evident with a larger charge [7,9,10]. A first set of fine jets extrudes from the outer edge upon the reflection of the shock wave, which is to be overtaken and overlapped by a second set of much larger jets from the inner edge. Hereinafter the first set of jets is referred to as minor jets, and the second set of jets as major jets. Understanding what determines the formation of this dual jetting, as well as the number and size of jets entails the knowledge pertaining to the actual physical mechanisms involved in the explosively driven fragmentation of granular materials. Several studies attributed this dual jetting phenomenon to the Richtmyer-Meshkov (RM) instabilities originating from the perturbations at the outer and inner edges of the charge [1,2,6]. The initial disturbances are normally known to be imposed by the rupture of the outer case. But the fragmented outer case has been observed to separate from the particle surface upon the arrival of the blast wave at the outer edge, in a similar fashion to a spallation layer [2]. Moreover the timescale for the RM instabilities to grow up to the discernable macroscopic features is much

[a] e-mail: xuekun@bit.edu.cn

longer than the shock interaction timescale corresponding to the formation of jets [4,9]. Therefore increasing efforts are being focused on the bulk fracturing of the particle bed under interaction with shocks [5,7,8]. In this work, the interactions between shock waves, the particle bed and the expanding detonation gases are numerically investigated via the hydrodynamic simulations. The calculations reproduce the radial density profiles of particle shell resembling those detected by the flash radiography [1], and more importantly reveal that the initial consistent particle shell evolves into an inner compact layer and an outer dilute layer which undergo differing evolvement. The formation of dual jetting structure presumably arises from the respective fragmentation of these two particle layers. Our earlier work [8] investigated the late-time fragmentation of the inner particle layer and associated it with the competition between the destabilizing viscous forces and the stabilizing inertial forces. This work will focus on the physical mechanism responsible for the spallation of the outer particle layer.

Given that powders, slurries, and liquids dispersed by explosive all exhibit a similar jetting structure but with distinctive features [1,4,6–8], a universal mechanism may well dominate the fragmentation of all these liquid-like materials but meanwhile varies with the distinct material features. A micromechanical approach describing the cavitation process originally applied to ductile damage in solids [11,12] has been proposed to account for the spallation in a liquid (or melt metal) subjected to a pulsed tensile load of duration τ [13,14]. The spall strength and the surface tension are among the key parameters controlling the cavitation process. The nucleation of voids corresponding to the spall damage initiation takes place upon the dynamic tensile strength reached. Meanwhile surface tension acts to damp the growth of voids and leads to a dissipation of a major part of the kinetic energy transferred to the material. Contrasting with solids and liquids, particles cannot support tensile stress or only moderate tensile stress with the presence of interstitial fluids. Neither do particles have surface tensions. It imposes a formidable challenge to adapt the previous cavitation model to account for the fragmentation of the particle bed. Besides, during the dilation upon the release wave the particle bed undergoes a drastic transition from the tightly compacted solid state to a dense granular flow, and then to the gaseous regime. The response of particles correspondingly varies dramatically [15,16], which should be properly taken into consideration. In this work, a three-phase cavitation model is put forth to describe the nucleation and growth of voids conditioned by the surrounding particles flows. The comparison between the experimental data and the theoretically predicted fragmentation onset as well as fragment size is carried out to validate the cavitation model.

Wet particles are observed to generate much more particle jets than dry particles [4,7–9]. Incorporating the moisture effect into the material model [17,18], the cavitation model predicts noticeably smaller fragments of saturated particles than those of dry particles. The marked dependence of the fragment size on the moisture content stems from the variation in the interaction between the shock wave and particles caused by the interstitial fluids. At high pressures, water is trapped within the interparticle pores effectively reducing the compressibility of wet particles. Thus less explosion energy is dissipated through irreversible compaction of particles and the transferred impulse is stronger with increased levels of moisture content. Wet particles subsequently undergo a higher strain rate dilation. An analysis analogous to the Mott cylinder model [19] is proposed to understand the relationship between the strain rate and the spacing between the neighboring voids.

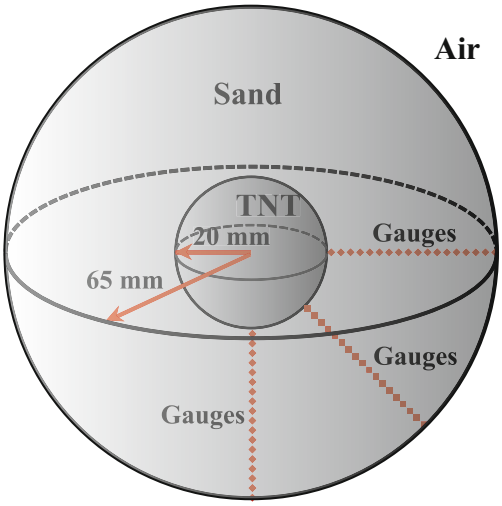

Fig. 1. Schematic of the numerical model setup to study the explosive disperse of the sand shell.

In this work, the evolvement of the dry and saturated particle beds subjected to the detonation of central explosives is numerically investigated in sect. 2. Based on the simulation results, sect. 3 identifies two distinct particle layers whose fragmentation is responsible for the formation of each set of jets. A cavitation model is established in sect. 4 to account for the physics involved in the jetting of the outer particle layer, which predicts a jet size comparable to the experimental results. Section 5 presents a discussion about the moisture effect on the particle jetting. Main conclusions can be found in sect. 6.

2 Evolvement of particle layers subjected to shock loading

2.1 Setup of the numerical model

Numerical simulations were performed to elucidate the interactions between particles, shock waves and detonation product gases. All the calculations in this section were carried out using AUTODYN 3D, a general purpose non-linear hydrodynamic modeling and simulation software [20]. The problem analyzed in the present study is the spherical charge in which either dry or saturated sand surround the central spherical explosive (TNT). The geometry of the charge is identical to the one investigated

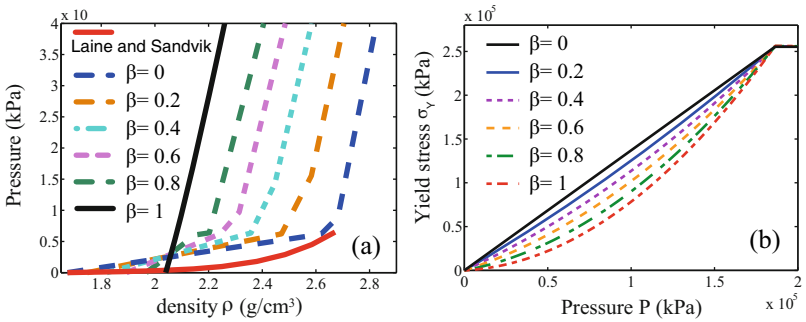

Fig. 2. EOS curves of the sand with varying degrees of saturation (a); variations in dependence of sand's yield stress on the pressure with increasing moisture contents (b).

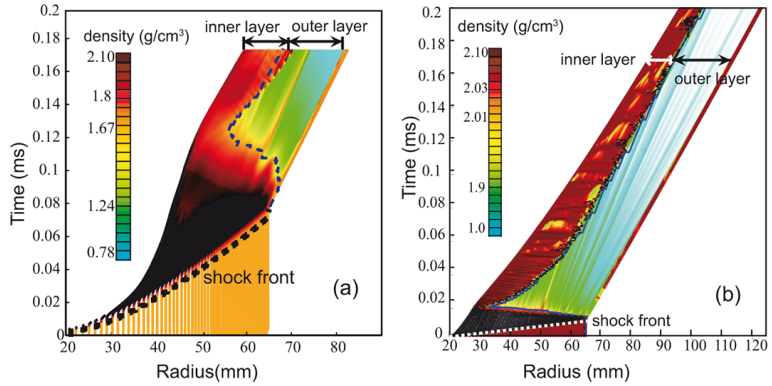

Fig. 3. Temporal variations in the density profiles of the dry (a) and saturated (b) sand shell.

experimentally in ref. [8] (see fig. 1). The Lagrangian processor was used to model the sand. High-energy explosives (TNT), gaseous detonation products and the surrounding air were modeled using the multi-material Eulerian processor. Different regions of the charge model were allowed to interact and self-interact using the AUTODYN interaction options. The "flow-out" boundary conditions were applied to all the outer boundaries of the air-filled portion of the computational domain. Three sets of 20 movable gauges were employed to monitor the transient density, velocity and pressure profiles of the sand shell.

2.2 Material constitutive models

The ideal gas and Jones-Wilkins-Lee types of equation of state were applied to air and TNT, respectively. The values of all the material parameters for air and TNT are available in the AUTODYN materials library. The original compaction model for sand in AUTODYN proposed by Laine and Sandvik [21] neglects the effects of the moisture content in the sand, therefore fails to describe the dynamic responses of wet sand with different degrees of saturation, β. Grujicic *et al.* [17,18] developed a modified version of Laine and Sandvik model to account for the effect of moisture content via explicitly incorporating the degree of saturation in the equation of state (EOS) and the strength model. At high deformation rates (of the order of $1.0 \times 10^5\,\mathrm{s}^{-1}$) and pressures (of the order of ca. 1 GPa) which are typical of the explosive loading, water/air is trapped within the sand pores and the deformation of the sand is controlled by the deformation of the three constituent phases. Given the relative incompressibility of the water phase, the compressibility of the wet sand is increasingly reduced with the degree of saturation as illustrated by the EOS of the wet particles with varying saturation (see fig. 2(a)). Besides, the wet sand's yield stress is reduced due to the moisture induced interparticle lubrication effects leading to a reduced effective friction coefficient. Figure 2(b) shows how the increasing degree of saturation alters the dependence of the yield stress on the pressure. For details of the modified compaction model, readers can be referred to refs. [17,18]. This model has been validated by the comparison with a number of buried-land mine blast experimental results [9,13].

2.3 Numerical results

The evolvement of the sand shell upon blast wave can be well embodied by the variations in its radial density profile as shown in fig. 3. The sequence of events basically resembles those occurring in the shock loaded water shell described by Milne *et al.* [4]. After detonation of the central explosive at time zero, a spherical shock wave travels outwards compacting the surrounding particles. The arrival

of the shock front invokes the immediate jump of the density as indicated by the coincidence between the trajectory of the shock front and the division line between the initial density and the compacted one (see fig. 3). When the wave reaches the surface of the sand shell, it is partially transmitted to the air as a blast wave and partially reflected as an expansion wave tearing a thin outermost layer from the outer edge of the sand shell. The expansion wave progresses inwards and effectively relieves the pressure. A substantial dilation of the sand ensues. The sand restores its initial density at the end of the unloading and continues inertial expanding with the increasingly decreased density. Compression waves induced by the expansion of gaseous detonation products in the meanwhile propagate outwards from the inner edge. They may well counter and arrest the inward advancing release waves sparing the tightly compact inner particle layer from being dispersed, which exactly is the case for dry sand. On the contrary, the release waves in the saturated sand travel so fast leaving the entire particle bed dilated throughout that the late-time compression waves have to re-collect and compact the loose particles beginning from the inner edge. The compact inner particle layer either maintained or regenerated by the compression waves initially gathers up some loose particles, but soon tails behind the rapidly expanding outer layer which is in the gaseous state by then.

As the result of the complex interactions with the shock wave, the reflected tensile waves and the compression waves, both dry and saturated particle shells laminate into the inner and outer particle layers with distinct densities. The rapidly diluting outer particle layer is analogous to the high-density foam-like water layer sandwiched between the spall layer and the intact inner water layer identified by Milne *et al.* [4]. The inner particle layer conversely remains compact and intact for a much longer time. During the computational timescale, no appreciable density decrease within the inner particle layer can be detected.

Despite the alike double layer structure both the dry and saturated sand shell evolve into, some prominent differences are worth noting. Specifically, the unloading duration of the outer particle layer in the saturated sand is one order less than that in the dry sand. As a matter of fact, low compressibility of the saturated sand inhibits the explosion energy dissipation through the irreversible compaction of grains so that promotes more energy converted into the kinetic energy and the reversible elastic energy. The higher kinetic energy contributes to the postponed fragmentation of the inner particle layer [8]. On the other hand, larger elastic energy and faster moving release waves in the saturated sand give rise to a significantly elevated dilation rate. The dilation rate is the essential parameter controlling the spallation of the outer particle layer as will be discussed in sect. 4.

3 Formation of the dual jetting

As indicated by the evolution of the density profile, within the time of the order of the shock interaction timescale the density of the outer layer drops to the level of the gaseous state implying a complete disintegration. Many experimental studies [1–6,8] likewise perceived the shock interaction timescale as the characteristic timescale associated with the incipient jetting. This early-time disintegration of the outer particle layer accordingly corresponds to the formation of minor jets. By contrast, the fragmentation of the compact inner particle layer will presumably occur in the late time when the influences of the compression waves and the fragmented outer particle layer diminish. Although the formation time of the major jets emerging in later time is experimentally hard to access, it most likely stems from the late-time fragmentation of the compact inner particle layer. The formation of these two distinct particle layers and the respective fragmentation occurring at different time are schematically illustrated by fig. 4(a)-(c) and (d)-(f), respectively.

Our earlier work [8] addressed the fragmentation of the compact inner particle layer which is modeled as an incompressible viscous fluid shell. The inner interface of the shell expands outward at a constant velocity. This theory favors a bulk instability arising from the competition between the stabilizing inertial forces and the destabilizing viscous forces. The inertial forces are a function of the circumferential strain and the shell characteristic length. The viscous forces characterized by the yield stress vary with the degree of saturation as evidenced by the varying pressure dependence of the wet sand's yield stress (see fig. 2(b)). Consequently this expanding shell model can take into account the blast loading, the geometry of the charge and the nature of the granular material as well. The shell thickness upon the instability onset provides a first-order estimate of the fragment size, specifically the size of large fragments evolving into the major jets in the late time (see fig. 2(d)-(f)).

The hypothesis of the incompressibility appropriate for the compact inner particle layer does not hold for the outer particle layer which dilates instantly upon the release wave. The fact that the dilating particle layer disintegrates into particle agglomerates opposed to a cloud consisting of constituent grains precludes decohesion as a candidate mechanism. Although studies about spallation of unbound granular materials are comparatively scarce due to the rapid evolvement of particle fragments and the lack of adequate experimental techniques, the widely studied cavitation model responsible for the spallation of metallic glasses [12,13], another typical disordered matter, may shed some lights into the spallation of particle ensemble given the resembling packing structure (albeit on different length scales) and similarities of deformation in terms of highly localized shear bands [22]. The profuse inter-particle pores in granular materials can be seen as nucleation sites for potential cavities. Nevertheless the nature of voids nucleation and growth in particles starkly differs from that in metallic glasses as will be discussed in sect. 4. A cavitation model taking the unique behavior of particles into account is proposed in the section below and validated by comparing the theoretical predictions and experimental results.

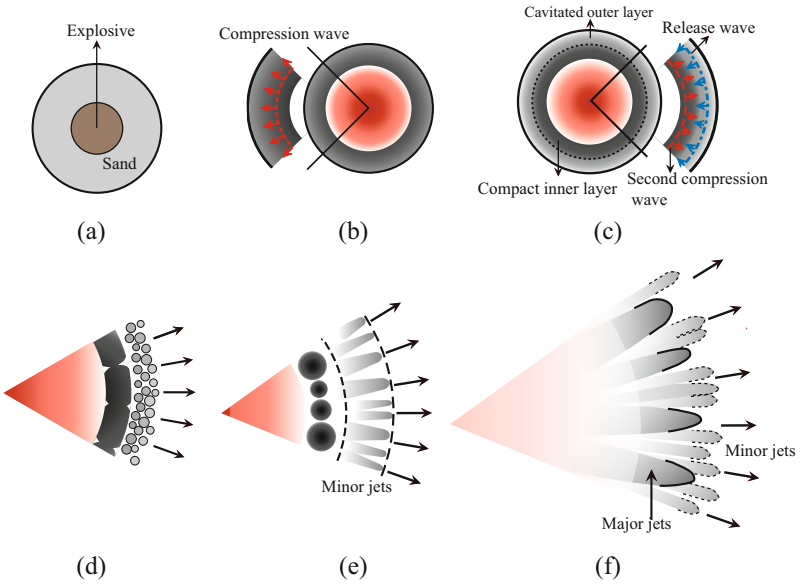

Fig. 4. Schematic of the evolvement of the shocked sand shell and the formation of the dual jetting.

4 Dynamic cavitation of compacted sand upon the release wave

4.1 Introduction of the cavitation model based on the expansion of the hollow sphere

The incipient spallation of the outer particle layer takes the form of a macroscopic dilation in the wake of unloading waves spreading behind the shock front. The dependence of the volumetric variation on the pressure is schematically plotted in fig. 5(a). Within the frame of the cavitation model, the bulk of the sample is seen as a collection of adjacent hollow spheres of internal and external radii $a(t)$ and $b(t)$ (see fig 5(b)), respectively [13]. In the case of the dry sand, the value of the initial inner radius of the hollow sphere a_0 is to guarantee that the initial porosity α_0, $\alpha_0 = a_0^3/b_0^3$ is consistent with the shock compacted density of sand. For the saturated sand within which no unfilled inter-particle pores exist, a_0 is chosen in such a way that the initial porosity α_0 is sufficiently small so that the saturated sand can be considered as initially intact. Clearly the value of a_0 in the dry sand is associated with the initial outer radius of the sphere b_0, which can be interpreted as the mean half-length between two neighboring nucleation sites as depicted in fig. 5(b). Signor *et al.* [11] suggested a critical value b_0 for the cavitation of the melt tin upon which viscous flows and surface tension consume all the kinetic energy transferred to the shocked material and therefore the cavity expansion is sustained. Nonetheless, particles cannot support surface tension and viscous flows (if they exist) in particles seem trivial in comparison with those in solids, therefore the void growth will inevitably become infinite due to lacking the adequate energy dissipation mechanism. This energy-based criterion is not appropriate in terms of choosing b_0 for the particle cavitation model. As b_0 defines the mass volume involved in the cavitation pattern, the "microscopic" pressure invoked by the cavitation varies with b_0 as will be seen in sect. 4.2. The "microscopic" pressure should agree with the "macroscopic" pressure dictated by the volumetric variation. This compatibility provides a criterion for the determination of b_0. Details of this criterion will be presented in sect. 4.2. To ensure that the expansion of the microscopic hollow sphere is compatible with the dilation of the macroscopic outer particle layer, the microscopic expansion rate of the sphere, $3\dot{b}/b$, should remain consistent with the macroscopic dilation rate of the particle layer, $\dot{V}/V$, where V is the volume of the outer particle layer. The dilation rates at these two length scales are thereafter detonated by a single parameter D.

The validity of the hollow-sphere pattern being representative of voids growth in the modeled volume requires a sufficiently uniform kinematical and thermodynamic state throughout the volume. This prerequisite is greatly restrictive in the case of strong transient loading like shock waves. Nonetheless the instantaneous dilation rates of subdomains at different radii collapse into one dilation rate *vs.* unloading time curve (figure not presented here), indicating a roughly uniform dilation throughout the outer particle layer. A rigorous pertinent examination has been presented by Dragon and Trumel [23].

4.2 Analytical formulation of the cavitation process

4.2.1 Formulation of the phase I

The first stage of the hollow-sphere expansion is prescribed by the relaxation of the accumulated pressure accompanied by the volumetric increase dictated by the dilatation rate D. This early stage is herein referred to as the phase I. Figure. 6 shows the temporal variations in the dilation rates of the dry (a) and saturated (b) sand

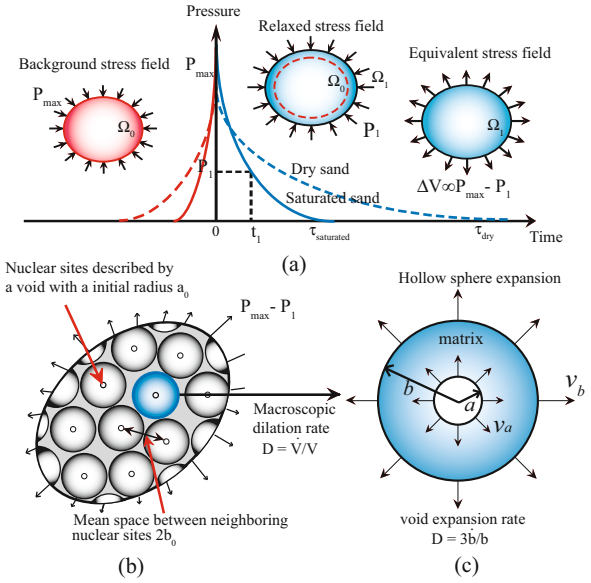

Fig. 5. (a) Pressure relaxation experienced by the dry (dashed line) and saturated (solid line) particle layer accompanied by the dilation; (b) schematic of the hollow-sphere pattern; (c) the expansion of the individual hollow sphere.

throughout the whole cavitation process. The dilation initiates upon the shock breakout at the free surface. Afterwards one observes a significant increase of the dilation rate, then a short plateau is followed by a gradual decrease. The phase I only accounts for a fraction of the whole cavitation process. Specifically the phase I of cavitation in the saturation sand only takes up the first 4% of the total cavitation time. It is worth noting that the dilation rate of the saturated sand is more than twice that of the dry sand, in line with the steeper shock and release fronts observed in the saturated sand (see fig. 2).

A homogeneous displacement field in the matrix of the hollow sphere results from both the bulk expansion and the growth of the void, as proposed by the following approximation [11,13]:

$$x_r^3 = \varphi(t)\left[r^3 + \omega(t)\right], \tag{1}$$

where $\varphi(t) = \rho_0/\rho$ denotes a dilation factor of the bulk matrix, $\omega(t)$ stands for the volumetric change of the void, $x_r(r,t)$ is the Lagrangian radius of a material particle with the radius r at time $t = 0$. The kinematical quantities (*e.g.* radial velocity v_r, acceleration γ_r, strain rate tensor d_{ij} and strain ε) can be derived from eq. (1).

The hollow-sphere matrix is modeled as a compressible and visco-plastic material. Thus the stress tensor in the matrix, σ_{ij}, can be partitioned into an isotropic part (pressure, P) and a deviatoric part (Newtonian viscous stress). The unloading of the compacted sand is of an elastic nature [18]. In this case, the P *vs.* ρ relationship is defined as [18]

$$\frac{\mathrm{d}P}{\mathrm{d}\rho} = C_0^2(\rho, \alpha_0, \beta_0), \tag{2}$$

where the speed of sound C_0 is a function of density, porosity of the compacted sand α_0 and degree of saturation β_0,

$$C_0(\mathrm{m/s}) = 1.988{\cdot}10^{-9}\rho_{\mathrm{quartz}}^{3.613}(\rho/\rho_{\mathrm{quartz}})^{3.613} + 476.46\alpha_0\beta_0. \tag{3}$$

The deviatoric stress is proportional to the deviatoric strain with the proportionality constant being equal to the shear modulus G. Due to the porous nature of sand, its shear modulus is taken to depend on its packing density, which is described by the following functional relationship [18]:

$$G(\mathrm{kPa}) = \begin{cases} 5.2175\times10^{-14}(\rho - \alpha_0\beta_0\rho_{\mathrm{water}})^6, \\ \quad \rho(\mathrm{kg/m^3}) < (1-\alpha_0\beta_0)\rho_{\mathrm{quartz}} + \alpha_0\beta_0\rho_{\mathrm{waver}}, \\ (1-\alpha_0\beta_0)G_{\mathrm{Bulk}}, \\ \quad \rho(\mathrm{kg/m^3}) \geq (1-\alpha_0\beta_0)\rho_{\mathrm{quartz}} + \alpha_0\beta_0\rho_{\mathrm{waver}}, \end{cases} \tag{4}$$

where $G_{\mathrm{Bulk}}(= 3.73470\times10^7)$ denotes the shear modulus of fully compacted dry sand. At fully compaction, the density of sand is equal to $(1-\alpha_0\beta_0)\rho_{\mathrm{quartz}} + \alpha_0\beta_0\rho_{\mathrm{water}}$. With the displacement field in eq. (1), one obtains

$$\begin{aligned}\sigma_{ij} &= -P\delta_{ij} + 2G\left(\varepsilon_{ij} - \frac{1}{3}\varepsilon_{kk}\delta_{ij}\right) \\ &= -P\delta_{ij} + 2G\begin{bmatrix} -\dfrac{2\varphi\omega}{3x_r^3} & 0 & 0 \\ 0 & \dfrac{\varphi\omega}{3x_r^3} & 0 \\ 0 & 0 & \dfrac{\varphi\omega}{3x_r^3} \end{bmatrix}. \end{aligned} \tag{5}$$

The spatial (Eulerian) form of the equation of balance of linear momentum is written with respect to the spherical symmetry of the present problem:

$$\frac{\partial\sigma_{rr}}{\partial r} + \frac{2}{r}(\sigma_{rr} - \sigma_{\theta\theta}) = \rho\gamma_r. \tag{6}$$

The reference configuration at time $t = 0$ is the compacted sand submited to the shock wave with the pressure front of $P_{\max}$. Due to the lack of capacity to support the tension, the void nucleation in particles is not initiated upon the tensile strength reached like the spall damage initiation occurring in solids and liquids. Instead, both the matrix dilation and the void nucleation occur upon pressure relaxation and are determined by the pressure decrement, $\Delta P = P_{\max} - P$, rather than the instantaneous pressure P. Thus subtracting the instantaneous pressure from the reference pressure, namely the maximum pressure exerted on the sand by the shock front, one can derive the effective hydrostatic pressure of the unloaded sand. Taking the above argument into account, one can give the boundary conditions at $x_r = b$ and $x_r = a$ by subtracting from the

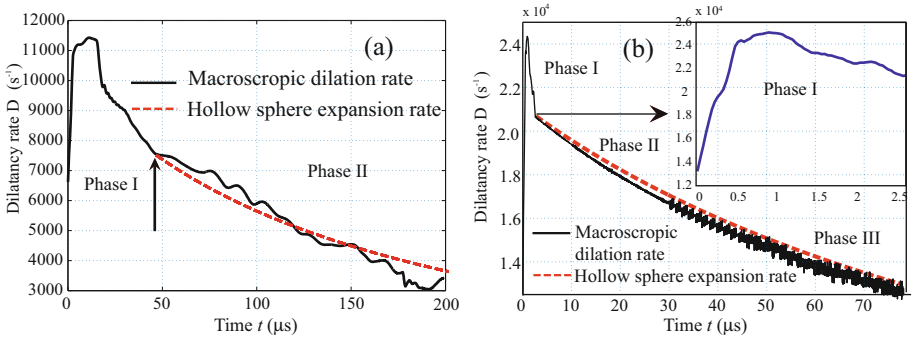

Fig. 6. Evolution of the dilation rate D during the cavitation process for the dry (a) and saturated (b) sand. The solid line represents the dilation rate obtained by the numerical simulation. The dashed line plots the approximated dilation rate based on the assumption that the outer boundary of the sphere expands outward at a constant velocity, $v_b(\tau)$, during the phase II and III.

background stress field in the reference configuration:

$$\begin{aligned}\sigma_{rr}(b) &= \Delta P - \frac{4G\varphi\omega}{3b^3}\,,\\ \sigma_{rr}(a) &= 0 \quad \text{for dry sand,}\\ \sigma_{rr}(a) &= \frac{2N_a}{a} \quad \text{for saturated sand,}\end{aligned} \tag{7}$$

where ΔP is the pressure decrement (with positive sign) acting as the effective tension, N_a is the surface tension ($\sim 0.05\,\mathrm{N/m}$) induced by the interstitial water. Equation (6) can be integrated from a to b by using the constitutive relation (5)

$$\begin{aligned}\Delta P &= \frac{4}{3}\frac{G\varphi\omega}{b^3} + \frac{4G}{3}\ln\left(\frac{b^3-\varphi\omega}{a^3-\varphi\omega}\cdot\frac{a^3}{b^3}\right)\\ &\quad + \int_a^b \rho\gamma_r \mathrm{d}x_r \quad \text{for dry sand,}\\ \Delta P &= \frac{4}{3}\frac{G\varphi\omega}{b^3} + \frac{2N_a}{a} + \frac{4G}{3}\ln\left(\frac{b^3-\varphi\omega}{a^3-\varphi\omega}\cdot\frac{a^3}{b^3}\right)\\ &\quad + \int_a^b \rho\gamma_r \mathrm{d}x_r \quad \text{for saturated sand.}\end{aligned} \tag{8}$$

The detailed expression for $\int_a^b \rho\gamma_r \mathrm{d}x_r$ does not appear in eq. (7) but can be derived from eq. (1).

During the phase I, the growth of the void is negligible so that inertial effects are assumed to have a minimum influence. The inertial term $\int_a^b \rho\gamma_r \mathrm{d}x_r$ is neglected in phase I. The only unknowns in eq. (8) are ω and φ. A first relationship between ω and φ is given by the displacement boundary condition corresponding to a dilation rate D

$$D = \frac{\dot V}{V} = \frac{\varphi\dot\omega}{b^3} + \frac{\dot\varphi}{\varphi}\,. \tag{9}$$

The second relationship is given by making use of the radial velocity at $x_r = b$ derived from eq. (1)

$$v_r(b) = \varphi\dot\omega + \dot\varphi(b+\omega). \tag{10}$$

The numerical simulations of the expanding sand shell subjected to the blast wave can render the radial velocity

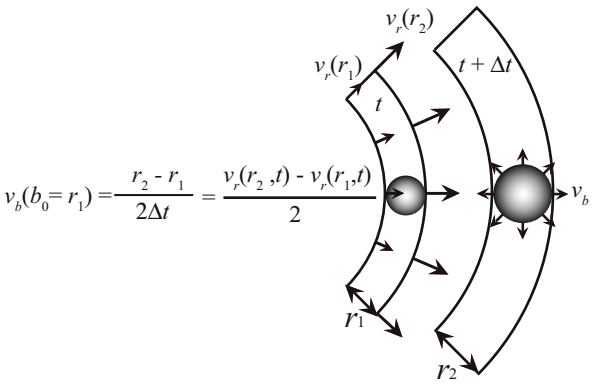

Fig. 7. Illustration of the derivation of the expansion velocity at the outer boundary of the sphere, v_b, from the velocity profile of the expanding velocity.

gradient leading to the dilation of the shell. Given that the shell, specifically the outer particle layer, is made up of an ensemble of hollow spheres, the expansion velocity at the outer boundary of the sphere, $v_b(b_0, t)$, can be derived from the velocity gradient of the shell as illustrated in fig. 7. $v_b(b_0, t)$ monotonously increases with the value of the outer radius of the sphere b_0 as shown in fig. 8, which is required by the compatibility between the macroscopic dilation and the expansion of the hollow sphere:

$$D = 3\frac{v_r(b)}{b}\,. \tag{11}$$

Again the expansion velocity of the hollow sphere in the saturated sand almost doubles that of the hollow sphere with the same outer radius in the dry sand (see fig. 8(a) and (b)), which is in line with the relationship of the dilatation rates in dry and saturated sand.

Initial conditions of the problem are $\varphi(0) = 1$, $\omega(0) = 0$, $\dot\varphi(0) = D$, $\dot\omega(0) = 0$ corresponding to the instantaneous response solely due to the bulk elasticity of the matrix. After solving the differential equations (8)–(11), one can compute from $\varphi(t)$ and $\omega(t)$ the "microscopic" hydrostatic pressure decrement $\Delta P_{\mathrm{micro}}$ and the porosity $\alpha = a^3(a_0, t)/b^3(b_0, t)$. Figure 9 gives the evolution

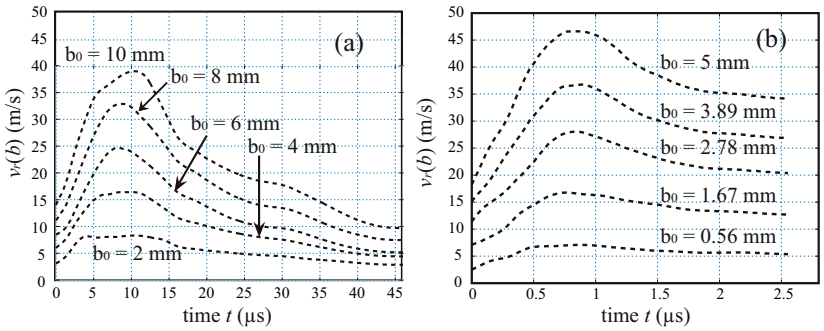

Fig. 8. Evolution of the expansion velocity at the outer boundary of the hollow sphere, $v_b(\tau)$, with varying outer radius in dry (a) and saturated (b) sand.

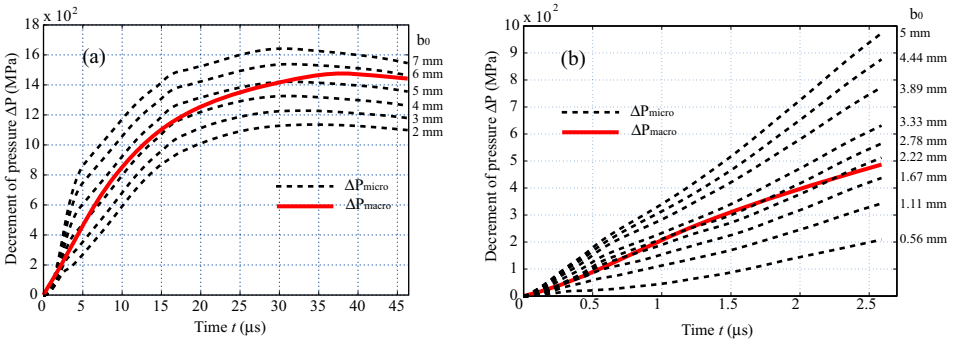

Fig. 9. Evolution of the "microscopic" (dashed curves) and "macroscopic" (solid curves) pressure decrements during the phase I of cavitation in the dry (a) and saturated (b) sand.

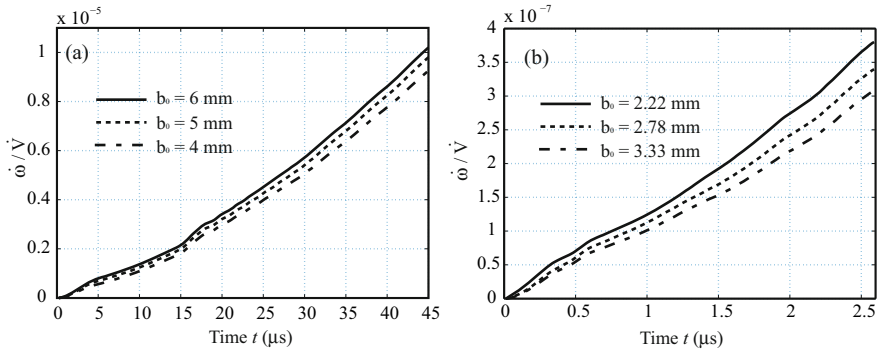

Fig. 10. Ratio of the growth rate of the void $\dot{\omega}$ and the volumetric increase rate $\dot{V}$ of the hollow sphere for the dry (a) and saturated (b) sand.

of ΔP_{micro} with varying b_0 during the beginning of the hollow-sphere expansion (phase I) in the dry (fig. 9(a)) and wet (fig. 9(b)) sand. ΔP_{micro} is elevated when more mass indicated by the increased b_0 is involved in each cavitation pattern.

During the phase I, voids hardly begin to grow due to the inertial resistance. This hypothesis is supported by the trivial proportion of the volumetric increase rate of the hollow sphere $\dot{V}$ contributed by the void growth $\dot{\omega}$ (see fig. 10). With the unloading particle layer being regarded as a homogeneous continuum, the macroscopic volumetric variation dictated by the dilation rate D prescribes the "macroscopic" pressure decrement ΔP_{macro} via the P *vs.* ρ relationship given by eq. (2). The evolution of the "macroscopic" pressure decrement ΔP_{macro} represented by the solid curves in fig. 9 is plotted against the evolution of a range of "microscopic" pressure decrement ΔP_{macro} (dashed curves) derived from the microscopic cavitation modeled by an ensemble of hollow spheres with varying outer radius b_0. The validity of the cavitation model requires the consistency between the "microscopic" and "macroscopic" pressure, which can serve as the criterion for determining $2b_0$, an estimate of the fragment size. As is evident from fig. 9, the appropriate range of values for b_0 is 4–6 mm and 1.6–3.3 mm for dry and saturated sand, respectively. The experiments pertaining to the explosive

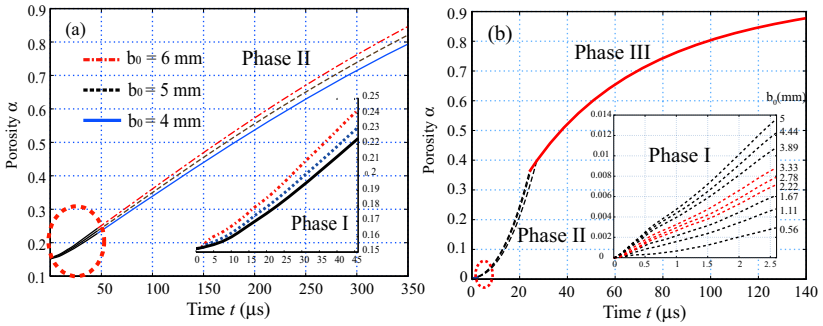

Fig. 11. Porosity evolution during the whole cavitation process for the dry (a) and saturated (b) sand.

dispersal of the cylindrical particles beds discerned a hundred plus minor particle jets around the perimeter and deduced that the initial particle fragment size is around 2–4 mm [4,6,9], which is quite close to our theoretical predictions. Furthermore, the smaller fragment size of the saturated sand predicted by the cavitation model is supported by the increased number of wet particle jets observed in experiments [4,6–8].

4.2.2 Formulation of phase II and III

The end of phase I of cavitation coincides with the fully relaxation of the pressure marked by the restoration of the initial packing density. Afterwards the rapidly expanding matrix progressively becomes gaseous so that the particles interact by collision and the continuous displacement/stress field does not exist. Thus the matrix and the void of the hollow sphere undergo the independent inertial expansion. The gaseous regime of the matrix is hereinafter detonated as the phase II of cavitation, which sustains as long as the matrix remains more dilute than the initial packing state. The outer and inner interfaces of the hollow sphere expand with the velocities at the end of the phase I, namely $v_b(\tau)$ and $v_a(\tau)$, respectively. The expansion rate of the sphere derived by eq. (11) shows a fairly good agreement with the macroscopic dilation rate (see fig. 5). In contrast to the insignificant increase of the porosity during phase I, phase II sees the substantial increase of the porosity (see fig. 11) resulting from the inertial expansion of voids.

A critical value of $\alpha_c(\sim 0.6\text{–}0.8)$ is assumed to be the fragmentation threshold. Note that if void coalescence takes place, the final stage of the fragmentation may also occur prematurely (for $\alpha < \alpha_c \sim 0.6\text{–}0.8$) by void linking. Examining the packing density of the matrix in the dry sand suggests that the gaseous state of matrix maintains even when the fragmentation starts. By contrast, the gaseous saturated sand is soon transformed into the dense granular flows when the loose particles get recompressed by the unconstrained outward expansion of the void. The subsequent expansion of the void, detonated as the phase III, is conditioned by the dense granular flow in the incompressible matrix.

The new displacement field in the incompressible matrix becomes

$$x_r^3 = r^3 + \omega(t). \tag{12}$$

In the dense granular flows regime, the deviatoric stress in particles, τ_{ij}, is proportional to the deviatoric strain rate [15,16]

$$\tau_{ij} = \nu_{\text{eff}} d_{ij}. \tag{13}$$

The effective viscosity ν_{eff} in eq. (13) depends on both the pressure and the shear rate

$$\nu_{\text{eff}} = \frac{\mu(I,\eta)P}{|d|}, \tag{14}$$

where $|d| = \sqrt{1/2 d_{ij} d_{ij}}$ is the second invariant of the shear rate tensor, the effective friction coefficient μ is a function of the inertial number I and the cohesion number η [15,16]

$$\mu(I,\eta) \simeq \mu_{\min}(\eta) + B(\eta) I. \tag{15}$$

The definition of the dimensionless numbers I and η can be found in appendix A. Considering the high strain rate and the sub-millimeter grain size involved in the explosive dispersal of particles, the value of I is close to zero, $I \to 0$, which approximates the quasi-static limit, $\mu \to \mu_{\min}$. The detailed expression of $\mu_{\min}(\eta)$ is presented in appendix A.

By employing the displacement field and the constitutive law of the incompressible matrix (eqs. (13)–(15)), integrating the momentum balance equation (eq. (6)) from a to b, one can get

$$\left(1 + \frac{2\sqrt{3}}{3}\mu + 2\sqrt{3}\mu \ln\frac{b}{q}\right) P = +\rho\left(\frac{\ddot{\omega}}{3}\left(\frac{1}{b} - \frac{1}{a}\right)\frac{\dot{\omega}^2}{18}\left(\frac{1}{a^4} - \frac{1}{b^4}\right)\right) - \frac{2N_a}{a}. \tag{16}$$

Based on the incompressibility hypothesis of the matrix and the assumption that the outer interface of the hollow sphere keeps the invariable velocity $v_b(\tau)$, one can calculate the volumetric increase of the void, ω, and its first- and second-order differentials. The pressure invoked by the outward impulse induced by the void expansion incomparable with the matrix expansion is a function of ω, $\dot{\omega}$, $\ddot{\omega}$, whose evolution is shown in fig. 12. As the re-compact

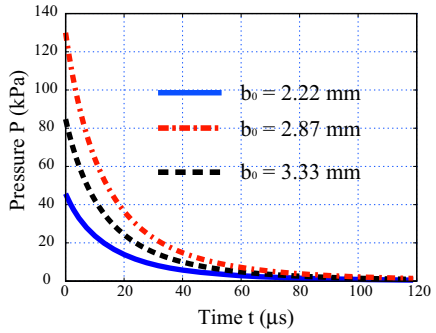

Fig. 12. Pressure evolution of the saturated sand during phase III.

granular matrix yields and the dense granular flows prevail to accommodate the thinning of the matrix shell, the pressure rapidly declines to the negligible level (see fig. 12) so that the expansion of the outer radius barely "feels" any disturbance caused by the granular flows inside the matrix.

The increase of porosity in the saturated sand during the phase II is increasingly accelerated until the transition to the phase III (see fig. 11) beyond which the void expansion is to be conditioned by the incompressible deformation of the matrix. Applying the above-mentioned fragmentation criterion leads to the estimation of the fragmentation onset of the outer particle layer, which occurs at 200–300 μs for the dry sand and 50–100 μs for the saturated sand after the detonation. Similarly Milne *et al.* [4] reported that the features at the outer edge of the sand shell subjected to the central explosion become discernable during the first several hundred microseconds.

Thanks to the low compressibility of the saturated sand, the majority of the shock energy transferred to the sand is elastically stored in the bulk rather than consumed on the particle compaction as occurs in the shock compaction of the dry sand. The release of the reversible elastic energy initiates and sustains the expansion of the void and the matrix. Thus, the larger the reversible elastic energy, the higher the kinetic energy acquired by voids. The cavitation process consequently progresses much faster in the saturated sand and the resulting fragmentation occurs earlier.

5 Discussion

Among several competing theoretical approaches being pursued to account for the spallation of the particle layers subjected to shock loadings [3,6,10], the cavitation model is capable of predicting the fragmentation onset and the fragment size consistent with the experimental results. Therefore cavitation is inferred here to be the most probable spallation mechanism of the outer particle layer. It is necessary to focus special attention on the parameter b_0, because $2b_0$ stands for the length between two activated nucleation sites and therefore provides an estimation for the fragment size. Given that all inter-particle pores are the candidates for the nucleation sites, there is surely a certain interaction between nucleation sites to suppress the activation of some nucleation sites. Otherwise the particle bed would be disintegrated into constituent grains instead of actual particle agglomerates. Moreover, the increased number of minor jets produced by the explosive dispersal of wet particles is indicative of the non-trivial role played by the interstitial fluids in the interaction between nucleation sites. Therefore the physics governing the interaction between two neighboring activated nucleation sites should take into account the pertinent moisture effect.

Mott put forth a Mott cylinder (or ring) as illustrated in fig. 13(a) to conceptualize how the interplay between two adjacent fractures determines the characteristic spacing of fractures [19]. The Mott cylinder is an idealization of an outward expanding cylindrical shell subjected to a uniform circumferential tension. Mott argued that release waves propagate away from sites of fracture relieving the tension and precluding the need for further fracture within the regions encompassed by tension release waves. The stress waves via which two separate fractures can communicate with each other are of essence in the dynamic fragmentation of solids as highlighted in the Mott cylinder model, and also play an equally vital role in the spallation of the particle bed. Nevertheless the nature of the stress waves and the propagation of waves in the dilating particle bed during the pressure relaxation differ starkly from those in the uniformly stretching solid cylinders (rings). Opposed to the tensile release wave emitted by the fracture in the Mott cylinder, the opening of voids in the dilating particle beds emanates compression waves compacting particles along the traveling path (see fig. 13(b)). The moderate compression of particles suffices to squeeze out the free space necessary for the void nucleation. As a consequence, any possible nucleation in the areas encompassed by compression waves is retarded. In the Mott cylinder, fragmentation is complete when fracture-induced release waves circumferentially subsume the entire cylinder. By contrast, compression waves in the particle bed cease as soon as the particle bed dilates to the gaseous state since afterwards there are no long-term particle contacts to transmit the stress. This coincides with the beginning of the phase II of cavitation. Taking into account the roughly equal nucleation probability at any inter-particle pore, any areas uncovered by the compression waves at the end of the phase I would allow for the additional void nucleation. Consequently all the area should be subsumed by compression waves by the end of the phase I. The combined travel length of the compression waves emanating from the neighboring nucleation sites can be taken as the upper limit of the spacing between nucleation sites, namely $2b_0$.

The dilating granular bed undergoes elastic unloading upon the release wave. The compression wave therein propagates at the speed of sound, C_0, which is a function of the instantaneous packing density (see eq. (3)). The total travel length of the compression wave, b_0, is proportional to the product of the speed of sound C_0 and the

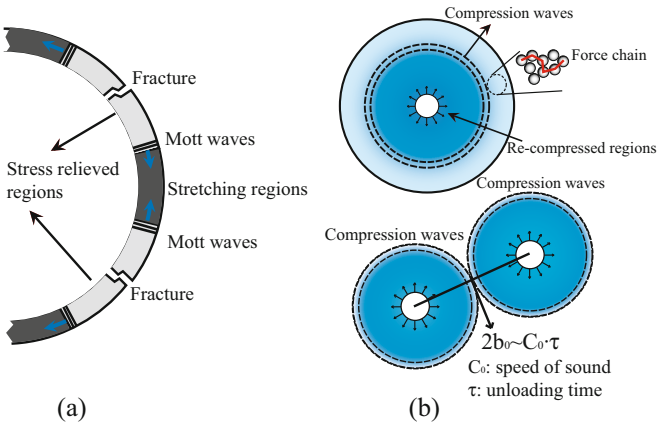

Fig. 13. (a) Schematic of the Mott cylinder model with regard to the dynamic fragmentation of the solid cylinder (ring); (b) In particles, compression waves propagate away from a activated nucleation sites (above) retarding any activation of the nucleation sites within the travel radius, and collide with those emanating from the adjacent nucleation sites.

unloading time, τ which is one order less in the saturated sand than that in the dry sand

$$b_0 \simeq \int_0^{\tau} C_0(\rho) \cdot t \, \mathrm{d}t. \tag{17}$$

Integrating $C_0(\rho)$ over the time τ one obtains

$$\begin{aligned} b_{0,\mathrm{dry}} &= 54.5\,\mathrm{mm}, \\ b_{0,\mathrm{saturated}} &= 5.3\,\mathrm{mm}. \end{aligned} \tag{18}$$

The upper limit of the spacing between neighboring voids in the dry sand is almost ten times that in the saturated sand, indicating the dominant effect of the unloading time τ. The adjacent nucleation sites may well be activated almost simultaneously so that the collision of the compression waves emitting from these sites takes place well before the pressure is fully relaxed. Thus the fragment size predicted by the cavitation model is well below the upper limit given by eq. (18).

6 Conclusion

As a result of interactions with various waves, the particle shell with uniform density throughout evolves into inner and outer particle layers undergoing distinct evolution. The spallation of the outer particle layer upon the reflected release wave ejects minor jets later being overlapped by major jets arising from the late-time fragmentation of the inner particle layer. To account for the physics governing the spallation of the outer particle layer, we propose a three-phase cavitation model which takes into account the unique behavior of particles subjected to drastically changing loading conditions. This cavitation model is validated by comparing the predicted fragmentation onset and the fragment size with the experimental results. With less energy consumed on compacting less compressible saturated particles, the shock wave remains a sharper front than that propagating through the dry particles, so does the reflected release wave. A steeper release front indicates a shorter unloading duration associated with higher strain rates. At higher strain rate, spatially separate voids have less time to communicate with each other via stress waves and an increased number of voids is allowed to be activated leading to smaller fragments of saturated particles.

The authors would like to acknowledge the support from the National Natural Science Foundation of China (Grant 11302029).

Appendix A. Friction coefficient of the saturated sand in the dense granular flow regime

The apparent friction coefficient of the cohesive particles $\mu(I,\eta)$ invoked by the effective viscosity increases approximately linearly with the inertial number I with proportionality $B(\eta)$, starting from a minimum value $\mu_{\min}(\eta)$ as described by eq. (15) [16]. I compares the inertial time $\sqrt{m/P}$ with the shear time $1/|d|$

$$I = |d|\sqrt{\frac{m}{P}}, \tag{A.1}$$

where $|d|$ denotes the shear rate, m denotes the mass of the particle. The mass of the particle of sub-millimeter diameter is of the order of 10^{-6} kg. The typical pressure involved in the dense granular flow is of the order of 10^0–10^1 kPa (see fig. 12). With a shear rate $|d| \sim 10^3\,\mathrm{s}^{-1}$, we get $I \sim 10^{-2}$ which implies the quasi-static regime

$$\mu(I,\eta) \sim \mu_{\min}(\eta).$$

$\mu_{\min}(\eta)$ is a function of the dimensionless cohesion number η

$$\eta = \frac{N_{\mathrm{c}}}{P d_p^2}\,, \tag{A.2}$$

where the surface tension of the interstitial liquid N_{c} is of the order of $0.05\,\mathrm{N/m}$, the particle diameter d_p is of the

order of 10^{-4} m. Thus η ranges from the order of 10 to the order of 100 with the pressure declining from $\sim 10^1$ kPa to $\sim 10^0$ kPa. Accordingly $\mu_{\min}(\eta)$ ranges from 0.25 to 1.5. The dependence of $\mu_{\min}(\eta)$ on η can be found in ref. [16] (see fig. 6 in ref. [16]).

References

1. F. Zhang, D.L. Frost, P.A. Thibault, S.B. Murray, Shock Waves **10**, 431 (2001).
2. D.L. Frost, C. Ornthanalai, Z. Zarei, V. Tanguay, F. Zhang, J. App. Phys. **101**, 113529 (2007).
3. D.L. Frost, S. Goroshin, R.C. Ripley, F. Zhang, *Proceedings of the 21st International Symposium of Military Aspects of Blast and Shock, Jerusalem, Israel* (2010) p. 35.
4. A. Milne, C. Parrish, I. Worland, Shock Waves **20**, 41 (2010).
5. Y. Gregoire, F. David, P. Oren, AIP Conf. Proc. **1426**, 1623 (2011).
6. R. Ripley, L. Donahue, F. Zhang, AIP Conf. Proc. **1426**, 1615 (2012).
7. L.F. David, G. Yann, P. Oren, G. Samuel, Z. Fan, Phys. Fluids **24**, 091109 (2012).
8. K. Xue, F. Li, C. Bai, Eur. Phys. J. E. **36**, 1 (2013).
9. R.C. Ripley, F. Zhang, J. Phys: Conf. Ser. **500**, 152012 (2014).
10. V. Rodriguez, R. Saurel, G. Jourdan, L. Houas, Phys. Rev. E **88**, 063011 (2013).
11. C. Denoual, J.M. Diani, AIP Conf. Proc. **620**, 495 (2002).
12. X. Huang, Z. Ling, L.H. Dai, Int. J. Solid Struct. **50**, 1364 (2013).
13. L. Signor, A. Dragon, G. Roy, T. De Resseguier, F. Llorca, Arch. Mech. **60**, 323 (2008).
14. T. Rességuier, L. Signor, A. Dragon, G. Roy, Int. J. Fracture **163**, 109 (2010).
15. Y. Forterre, O. Pouliquen, Annu. Rev. Fluid Mech. **40**, 1 (2008).
16. P.G. Rognon, J.-N. Roux, M. Naaim, F. Chevoir, J. Fluid Mech. **596**, 21 (2008).
17. M. Grujicic, B. Pandurangan, B.A. Cheeseman, W.N. Roy, R.R. Skaggs, Shock Vibration **14**, 1 (2007).
18. M. Grujicic, B. Pandurangan, R. Qiao, B.A. Cheeseman, W.N. Roy, R.R. Skaggs, R. Gupta, Soil Dynam. Earthquake Engin. **28**, 20 (2008).
19. D.E. Grady, in *Shock Wave Science and Technology Reference Library*, Vol. **3** (Springer, Berlin-Heidelberg, 2009) pp. 1–108.
20. AUTODYN Release 12.1 User Subroutines Tutorial (ANSYS, Inc., 2009).
21. L. Laine, A. Sandvik, *Proceedings of the 4th Asia-Pacific Conference on Shock and Impact Loads on Structure* (CI-Premier PTE LTD, Singapore, 2001) pp. 361–368.
22. V.F. Nesterenko, M.A. Meyers, H.C. Chen, Acta Mater. **44**, 2017 (1996).
23. A. Dragon, H. Trumel, in *Proceedings of the 5th International Symposium High Dynamic Pressure* (C.F.A., Saint-Malo, France, 2003) pp. 267–283.